Chemosphere 371 (2025) 144061

Contents lists available at ScienceDirect

Chemosphere

journal homepage: www.elsevier.com/locate/chemosphere

Synergistic photocatalytic degradation of methylene blue and ibuprofen using Co_3O_4-Decorated hexagonal boron nitride (hBN) composites under Sun-like irradiation

Mariam Bouziani [a,*], Asmae Bouziani [b], Abdelghani Hsini [c], Claudia L. Bianchi [d,e], Ermelinda Falletta [d,e], Alessandro Di Michele [f], Gökhan Çelik [b], Robert Hausler [a]

[a] STEPPE, École de technologie supérieure, Montreal, Canada
[b] Chemical Engineering Department, Middle East Technical University, 06800, Ankara, Türkiye
[c] Laboratory of Advanced Materials and Process Engineering (LAMPE), Faculty of Science, Ibn Tofail University, BP 133, 14000, Kenitra, Morocco
[d] Department of Chemistry, Università degli Studi di Milano, Via C. Golgi 19, 20133, Milano, Italy
[e] Consorzio Interuniversitario Nazionale per la Scienza e Tecnologia dei Materiali (INSTM), Via Giusti 9, 50121, Florence, Italy
[f] Dipartimento di Fisica e Geologia, Universit'a degli Studi di Perugia, via A. Pascoli, 06123, Perugia, PG, Italy

HIGHLIGHTS

- Co_3O_4-Decorated hBN was synthesized via wet impregnation.
- Methylene Blue and ibuprofen were successfully degraded using Co_3O_4-hBN under Sun-like irradiation.
- The 1% Co_3O_4 loading showed the highest photocatalytic efficiency for both pollutants.
- Holes, $O_2^{\bullet-}$ and •OH are reactive species.

GRAPHICAL ABSTRACT

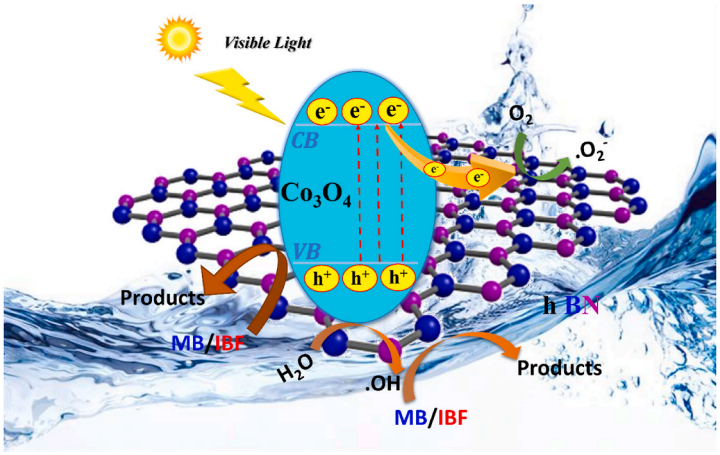

ARTICLE INFO

Handling Editor: Jun Huang

Keywords:
Co_3O_4
hBN
Nanocomposite
Sunlight irradiation

ABSTRACT

In this study, we report the synthesis and photocatalytic performance of Co_3O_4-decorated hexagonal boron nitride (hBN) composites for degrading methylene blue (MB) and ibuprofen (IBF) under sunlight irradiation. Using a dry impregnation method, the composites were prepared with varying Co_3O_4 loadings (0.5%, 1%, 2%). Comprehensive characterization confirmed the successful incorporation and uniform distribution of Co_3O_4 on the hBN matrix. Photocatalytic experiments revealed that 1% Co_3O_4-hBN composite exhibited the highest activity, achieving nearly 100% MB degradation in 60 min and 90% IBF degradation in 120 min. The enhanced

* Corresponding author.
E-mail address: mariam.bouziani.1@ens.etsmtl.ca (M. Bouziani).

https://doi.org/10.1016/j.chemosphere.2025.144061
Received 23 September 2024; Received in revised form 30 December 2024; Accepted 31 December 2024
Available online 8 January 2025

Degradation
methylene blue
Ibuprofen

photocatalytic efficiency is attributed to the synergistic effects between Co_3O_4 and hBN, which extend light absorption and promote charge separation. Our findings demonstrate the potential of Co_3O_4-decorated hBN composites as effective photocatalysts for environmental remediation. The study provides a foundation for further exploration of these materials, including their long-term stability and application to a broader range of pollutants.

1. Introduction

The increasing demand for clean energy and the need for effective environmental remediation strategies have driven extensive research into photocatalysis due to its potential for harnessing solar energy to drive chemical reactions (Herrmann, 1999; Hoffmann et al., 1995; Naciri et al., 2024; Rueda-Marquez et al., 2020). Photocatalytic materials, which facilitate these reactions, are crucial in these applications ranging from the degradation of organic pollutants in wastewater to the generation of hydrogen fuel through water splitting (Hashimoto et al., 2005; Jimenéz-Calvo et al., 2024; Li et al., 2016; Naciri et al., 2022). However, the challenge remains in identifying materials that are efficient and active not only under UV light but also and in particular under visible light, which constitutes the majority of the solar spectrum.

Recent advancements in material science have introduced innovative solutions for wastewater treatment, particularly through photocatalysis and adsorption techniques (Malik et al., 2023; Nazari et al., 2024). Metal-organic frameworks (MOFs) (Shah et al., 2024) and their composites, such as ZIF-8 (Ahmad et al., 2024; Nazir et al., 2025) and sulfur-doped MOF (Anum et al., 2023), have shown effectiveness in removing pollutants like nicotine and methylene blue dye. Similarly, biochar-based composites, including Delonix regia biochar-sulfur oxide (DRB-SO) (Eleryan et al., 2024), demonstrated high adsorption capacity towards dyes like methyl red and methyl orange.

Further advances in material engineering have resulted in advanced adsorbents, such as magnetic pomegranate peel-derived activated carbon (MG-PPAC), which efficiently removes dyes like Acid Orange 7 (Khalil et al., 2024). MOFs continue to play a significant role in wastewater treatment (Anum et al., 2024). In this regard, the recent advances in MOF membranes address synthesis challenges and broaden their application potential (Shahid et al., 2024). Additionally, MXene nanomaterials and MXene@MOF composites provide promising solutions for catalytic water splitting and wastewater remediation, leading to high materials' stability and great reactivity for diverse environmental applications (Afzal et al., 2024; Ullah et al., 2024).

Surprisingly, boron nitride (BN), known for its high stability under oxidative conditions, exhibits catalytic activity. (Grant et al., 2016). Since the paper by Grant et al. was published in 2016, the development of boron-based materials as catalysts has become a hot topic. Among various photocatalytic materials, hexagonal boron nitride (hBN) has attracted considerable interest in the field of photocatalysis due to its distinctive properties. With a wide bandgap of approximately 5.7 eV, hBN exhibits high thermal stability, chemical inertness, and excellent mechanical strength (Roy et al., 2021; Zhang et al., 2017; Zhou et al., 2018). These features make it an appealing candidate for harsh environmental conditions. Nevertheless, the wide bandgap limits hBN's photocatalytic activity predominantly to the ultraviolet (UV) region, which accounts for less than 5% of the solar spectrum. Therefore, enhancing the visible light absorption of hBN is a critical step toward making it a performing photocatalyst for broader solar light-driven applications.

To overcome the intrinsic limitations of hBN, various strategies have been explored, including doping with elements, defect engineering, and coupling with narrow-band gap semiconductors (Sheng et al., 2019; Zhou et al., 2018). Among these approaches, coupling with a visible light-active semiconductor seems to be particularly promising. Among the others, cobalt oxide (Co_3O_4) stands out as a suitable candidate for this purpose due to its narrow bandgap ranging between 1.5 and 2.75 eV, which allows it to absorb visible light effectively (Subagyo et al., 2023; Zhao and Ma, 2023). Additionally, Co_3O_4 possesses favorable redox properties and has been widely studied for its catalytic activity in various reactions, including oxygen evolution and reduction. The integration of Co_3O_4 with hBN leads to the formation of an interesting composite material with enhanced photocatalytic activity, surpassing the sum of their individual contributions. This synergy extends the photocatalytic activity across a broader range of the solar spectrum beyond what could be achieved with a simple mixture of the two components.

In this study, we report the synthesis and characterization of Co_3O_4-decorated hBN composites using a dry impregnation method. The effect of varying Co_3O_4 loadings on the structural, optical, and photocatalytic properties of the composites was systematically investigated. The fabricated composites were thoroughly characterized to elucidate the changes in the crystal structure, chemical bonding, optical properties, and electronic states induced by Co_3O_4 incorporation. The photocatalytic performance of the composites was evaluated through the degradation of two model molecules of two important categories: methylene blue (MB), dyes, and ibuprofen (IBF), drugs, under simulated sunlight, with a particular focus on understanding the role of Co_3O_4 in enhancing the visible light activity of hBN. Our findings demonstrate that the introduction of Co_3O_4 into hBN not only improves the visible light absorption but also enhances the photocatalytic efficiency of hBN, making the Co_3O_4-hBN composites promising candidates for solar light-driven environmental remediation and energy conversion.

2. Materials and methods

Cobalt acetate $Co(CH_3COO)_2.4H_2O$ was selected as a precursor for the cobalt dry impregnation and was purchased from Sigma Aldrich. The h-BN used in this study was commercial (99.9% metals basis) and also obtained from Sigma-Aldrich. Methylene Blue (MB, 97%) and Ibuprofen (IBF, ≥98 %) were selected as organic pollutants and purchased from Aldrich.

2.1. Synthesis

Co_3O_4 was incorporated into hBN using a wet impregnation method (Scheme S1 in SI). Solutions of $Co(CH_3COO)_2.4H_2O$ at different Co_3O_4 loadings (0.5%, 1%, and 2% by weight (%wt)) were prepared in deionized water. These solutions were dropwise added into the hBN powder with continuous stirring until saturation to ensure uniform distribution. The resulting mixtures were dried overnight at 80 °C and then calcined at 500 °C for 3 h to obtain Co_3O_4-hBN composites. Pristine Co_3O_4 was prepared first by dehydrating $Co(CH_3COO)_2.4H_2O$ at 120°C for 2h then calcined at 500 °C for 3 h.

2.2. Characterization

To identify the phases present in the pristine and composite samples, X-ray diffraction (XRD) analyses were conducted using a PANanalytical 'X'Pert PRO X-ray diffractometer. The measurements were performed using Cu Kα radiation (1.54060 Å) at a nominal power of 40 kV × 40 mA, with diffraction angles (2θ) ranging from 10° to 80°. Peak identification was achieved by comparing peak positions and intensities with data from the Joint Committee on Powder Diffraction Standards (JCPDS) database. The crystallite size (d) of the obtained samples was

calculated from Scherrer formula (Eq. (1)) (Shiraishi and Inagaki, 2003)

$$d = \frac{K\lambda}{\beta \cos \theta} \quad \text{Eq.1}$$

Here, K represents a constant, λ denotes the X-ray wavelength (0.15406 nm), β is the adjusted full width at half maximum (FWHM) in radians, and θ is the Bragg angle.

To examine the physical properties of the prepared samples, N_2 adsorption-desorption isotherms were recorded at −196 °C using a Micromeritics Tristar II 3020 instrument. Prior to these measurements, the samples were degassed at 150 °C for 6 h to remove any adsorbed moisture and to clean the pores. The specific surface area was calculated from the adsorption data using the Brunauer-Emmett-Teller (BET) method. The total pore volume was estimated from the amount of N_2 adsorbed at a relative pressure (P/P_o) of 0.98. Pore size distribution, pore volume, and pore diameter were determined using the Barrett-Joyner-Halenda (BJH) method. Fourier transform infrared spectroscopy (FTIR) was performed using a Mattson 1000 FTIR spectrophotometer. For the analyses, the samples were mixed with KBr and pressed into disks. The FTIR spectra were collected in transmission mode over a wavenumber range of 4000 to 500 cm^{-1}, with a resolution of 4 cm^{-1}. The optical properties and light absorption capacities of the composites were evaluated using a Varian-Cary 100 UV–Vis spectrophotometer equipped with an integrating sphere. $BaSO_4$ was used as a reference for these measurements. The optical bandgap energy was determined using the Kubelka-Munk function, as described in Equation (2) (Jaramillo-Páez et al., 2017):

$$A\left(h\nu - E_g\right)^{\frac{n}{2}} = \alpha h\nu \quad \text{Eq.2}$$

Here, α represents the absorption coefficient, h denotes Planck's constant, ν indicates the optical frequency, E_g stands for the band gap, and A is a constant. Both hBN and Co_3O_4 have an indirect band gap so n = 4. X-ray photoelectron spectroscopy (XPS) analyses were conducted with an X-ray photoelectron spectroscope PHI 5000 Versaprobe II, ULVAC-PHI (Inc., Kanagawa, Japan), using monochromatic Al Kα radiation (hν = 1486.6 eV). The binding energies (B.E.) were reported with an accuracy of ±0.2 eV. Peak fitting was performed using Gaussian−Lorentzian profiles, with background correction applied via the Shirley method. Binding energy calibration was done using the C1s peak at 284.6 eV.

The morphology of the samples was examined using scanning electron microscopy (SEM) with a Zeiss LEO 1525 field emission microscope equipped with an Inlens detector. Prior to imaging, the samples were metalized with chromium. Additionally, Energy Dispersive X-ray Analysis (EDX) was carried out using a BRUKER system.

Transmission electron microscopy (TEM) images were obtained with a Philips 208 transmission electron microscope. Sample preparation involved placing a small drop of the aqueous dispersion on a copper grid coated with a Formvar film, which was then allowed to evaporate at room temperature.

2.3. Photocatalytic tests

The photocatalytic performance of both pristine hBN and Co_3O_4-hBN composites with varying Co_3O_4 weight ratios was evaluated by examining the degradation of methylene blue (MB) and Ibuprofen (IBF) under simulated sunlight. MB, a dye widely used in industries like textiles, and IBF, a commonly used pharmaceutical, were selected as model pollutants due to their prevalence in wastewater and environmental persistence. Their distinct chemical properties and ease of detection make them ideal for evaluating the photocatalytic performance of the synthesized materials under simulated sunlight. The photocatalytic tests were carried out in a batch setup using a 250 mL Pyrex reactor wrapped with aluminum foil. The reactor was filled with 100 mL of an aqueous solution containing MB or IBF (10 ppm) and the photocatalyst (1 g/L). An Osram Ultra-Vitalux lamp (300 W), emitting a spectrum similar to sunlight with a peak in the UVA range at 365 nm, was employed for irradiation. Throughout the experiment, the lamp was positioned 10 cm above the surface of the MB or IBF solution. To maintain a constant temperature during the process, the batch reactor was equipped with a circulating water jacket. Prior to irradiation, the suspension was stirred in the dark for 20 min to establish adsorption-desorption equilibrium between the catalysts and the pollutant. The photocatalytic reactions were conducted for a total duration of 120 min for all samples. At designated intervals, portions of the suspension were taken, filtered through a 0.45 μm RC filter, and analyzed. The concentration of MB was determined by measuring the intensity of its absorption peak at λ_{max} = 664 nm, while the concentration of IBF was measured by HPLC (Shimadzu). The analysis was performed using a C18 column with dimensions of 4.6 mm × 150 mm and a particle size of 5 μm. The UV detector was set to 223 nm. The mobile phase was composed of water (adjusted to pH 2 with phosphoric acid) and methanol in a 1:4 ratio (v/v), flowing at a rate of 1.0 mL/min. The column was maintained at a temperature of 50 °C. For comparison, the photolysis of MB and IBF in the absence of a catalyst was also assessed under illumination.

2.4. Identification of active species

Radical scavenging experiments were conducted to identify the active species involved in the photocatalytic degradation process. Potassium iodide (KI, 0.3 mM), chloroform ($CHCl_3$, 2.4 mM), and isopropyl alcohol (C_3H_8O, 0.5 mM) were used as scavengers for holes (h^+), superoxide radicals (●O_2^-), and hydroxyl radicals (OH●), respectively. These scavengers were added to a solution of MB containing 1% Co_3O_4-hBN composite, and the experiments were carried out under simulated sunlight, as previously described.

3. Results and discussion

3.1. Characterization

The XRD patterns in Fig. 1A compare the crystalline phases present in Co_3O_4, hBN, and 1% Co_3O_4-hBN, selected among the others for its higher photocatalytic activity. The XRD pattern of hBN presents the characteristic peaks at around 26.6°, 41.6°, 43.8°, 50.2°, 55.1°, and 75.9° (01-085-1068) confirming the presence of hexagonal BN (Zhang et al., 2017). Furthermore, Co_3O_4 displays diffraction peaks at around 31.3°, 36.8°, 44.8°, 59.4°, and 65.2°, characteristic of cobal oxide in cubic phase (01-080-1541). Additionally, in the XRD pattern of 1% Co_3O_4-BN composite, only the diffraction peaks of hBN are present, as expected due to the low amount of Co_3O_4. The average crystallite sizes determined using the Scherrer equation are presented in Table 1. It is worth noting that the crystallite size increased after adding Co_3O_4, suggesting a good dispersion of cobalt oxide on hBN and potentially leading to efficient charge transfer and reduced recombination rates (Kadian et al., 2024).

The nitrogen adsorption-desorption analysis was carried out to obtain textural properties. The obtained results are given in Fig. 1B. All materials exhibit low N_2 adsorption at a low relative pressure region ($P/P_o < 0.1$), indicating the absence of micropores. A gradual increase was observed at a relative pressure between 0.1 and 0.8, indicating the presence of mesopores (Liu et al., 2016; Thommes et al., 2015). Co_3O_4 shows slightly higher adsorption compared to pristine BN and 1% Co_3O_4-BN, suggesting a larger surface area or better pore connectivity in Co_3O_4. At high relative pressure ($P/P_o > 0.8$) a sharp increase in adsorption was observed, forming a hysteresis loop, suggesting mesoporous materials (Thommes et al., 2015). The obtained isotherms for the 3 materials are classified as Type IV according to the IUPAC. Furthermore, the BET surface area, pore volume, and size for the 3 samples were measured, and the results are summarized in Table 1. 1% Co_3O_4-hBN maintains a pore volume and surface area close to that of pure hBN,

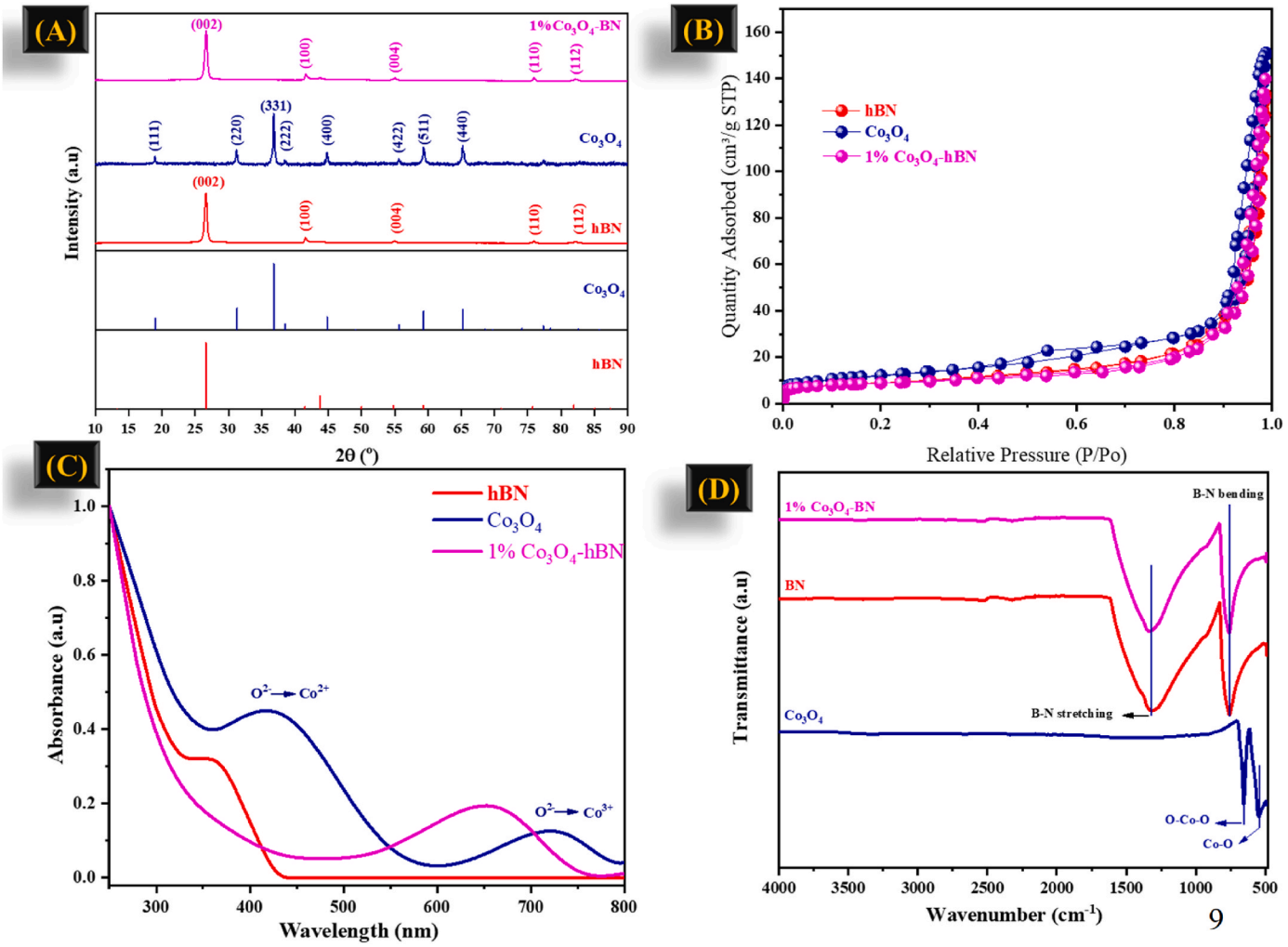

Fig. 1. (A) XRD patterns, (B) Nitrogen adsorption-desorption isotherms, (C) UV–Vis spectra, (D) FTIR spectra of hBN, Co_3O_4, and 1% Co_3O_4-hBN.

Table 1
Physicochemical properties and band gaps of hBN, Co_3O_4, and 1% Co_3O_4/hBN composites, respectively.

Samples	Crystallite size D (nm)	S_{BET} (m^2/g)	Pore volume (cm^3/g)	Pore size (nm)	Eg (eV)
hBN	16.0	31.0	0.20	25.0	5.9
Co_3O_4	25.7	42.5	0.23	18.8	1.5 2.8
1% Co_3O_4/ hBN	29.8	30.3	0.21	30.3	2.8

indicating that the introduction of Co_3O_4 does not significantly block the pores and decrease the surface area. However, the pore size shows an increase after the addition of Co_3O_4, which can be advantageous for photocatalytic reactions by improving the accessibility of reactants to the active sites. It is worth mentioning that the increase in pore size for the 1% Co_3O_4-hBN composite can enhance photocatalytic activity by improving light penetration and reactant diffusion.

The UV–vis diffuse reflectance spectra (DRS) were performed to analyze the spectral characteristics and optical properties of the synthesized samples. The results are reported in Fig. 1C. As expected, the Co_3O_4 spectrum shows significant absorbance in both the UV and visible regions. The absorbance features in the visible region are due to O^{2-} to Co^{2+} and Co^{3+} transitions (Liu et al., 2016). In contrast, hBN exhibits a high absorbance only in the UV region (~200–300 nm) (Gao et al., 2014; Liu et al., 2018). Furthermore, the 1% Co_3O_4-hBN composite displays a combination of the absorbance features of both BN and Co_3O_4. A slight shift in the absorbance peaks of hBN after Co_3O_4 addition was observed. This shift could indicate an interaction between hBN and Co_3O_4, leading to modified electronic properties and potentially better performance in photocatalysis. The bandgap energy of the obtained samples was calculated using the Tauc plot (Fig. S1), with the results presented in Table 1. The Eg of hBN is around 5.9 eV, in accordance with the values reported in the literature (Gao et al., 2014; Liu et al., 2018). The Tauc plot of Co_3O_4 displays two band gap energies (Fig. S2). The highest value (2.75 eV) is due to the transition $O^{2-} \rightarrow Co^{2+}$ (excitation from the valence to conduction band), whereas the lower value (1.5 eV) is attributed to $O^{2-} \rightarrow Co^{3+}$ transition (Co^{3+} is located under the conduction band) (Liu et al., 2016). A sub-band situated inside the energy gap is due to the presence of Co^{3+} centers in Co_3O_4 (Liu et al., 2016; Wang et al., 2009). The insertion of 1% of Co_3O_4 into hBN enhanced the optical properties of the photocatalyst, resulting in a narrow band gap (Fig. S3) (2.8eV). The narrowing of bandgap energy could improve visible light harvesting, and thus, high photocatalytic efficiency can be expected for composite samples. The photoluminescence (PL) spectrum of pristine hBN (Fig. S4) mainly appears in the UV region, reflecting its wide bandgap (~5.8 eV) and limited interaction with visible light, which restricts its photocatalytic activity to UV light, as noted in previous studies (Qanbarzadeh et al., 2023). In contrast, the PL spectrum of Co_3O_4 (Fig. S5) exhibits strong emission in both UV and visible regions, reflecting its broad light absorption and moderate bandgap (~2.1 eV), making it a suitable dopant for improving hBN's photocatalytic

efficiency. In fact, the 1% Co_3O_4-doped hBN shows a red shift in the PL spectrum (Fig. S6) towards the visible range (~400–450 nm), indicating enhanced visible light absorption. This enhancement is likely due to new defect states introduced by Co_3O_4 doping, which is consistent with findings from other studies on metal oxide-doped hBN (Fu et al., 2013; Zhou et al., 2022).

The FTIR analysis was carried out to identify the functional group present in hBN, Co_3O_4, and 1%Co_3O_4-hBN. The recorded spectra are given in Fig. 1D. The FTIR spectrum of Co_3O_4 displays a band in the range of 500 cm^{-1} and 700 cm^{-1}, typically associated with the Co–O stretching vibrations (Prabaharan et al., 2017). The FTIR spectrum corresponding to hBN shows a strong absorption peak at around 1400 cm^{-1}, ascribed to B–N stretching, and at around 800 cm^{-1}, belonging to B–N bending (Zhang et al., 2020). The 1% Co_3O_4-hBN sample displayed the same bands of hBN (around 1400 cm^{-1} due to the B–N stretching and at around 800 cm^{-1} related to the B–N bending). However, the absence of expected bands corresponding to Co_3O_4 could be explained by the amount of Co_3O_4 in the composite which might be too low for its characteristic peaks to be detected with sufficient intensity (Nakamoto, 2008).

The XPS survey spectrum of 1% Co_3O_4-hBN (Fig. S7) reveals the presence of B, N, and O elements from hBN, along with Co and O elements attributed to incorporating Co_3O_4 in the composite. These results confirm the successful addition of Co_3O_4 into hBN. The high-resolution XPS spectra for B1s, N1s, O1s, and Co2p are displayed in Fig. 2a-d. The B 1s spectrum for both pristine hBN (Fig. S8) and 1% Co_3O_4-hBN composite (Fig. 2a) shows a peak at around 190.4 eV, which corresponds to the B–N bonds in hBN (Shen et al., 2019). Similarly, the N 1s spectrum (Fig S8 and Fig. 2b) exhibits a peak at approximately 397.8 eV in both samples, characteristic of nitrogen in the hBN lattice (Shen et al., 2019). The Co2p spectrum (Fig. 2c) indicates the presence of cobalt in the composite, with peaks observed at approximately 780.3 eV and 795.6 eV, corresponding to the Co $2p_{3/2}$ and Co $2p_{1/2}$ core levels, respectively (Biesinger et al., 2011; Rana et al., 2020). These binding energies are

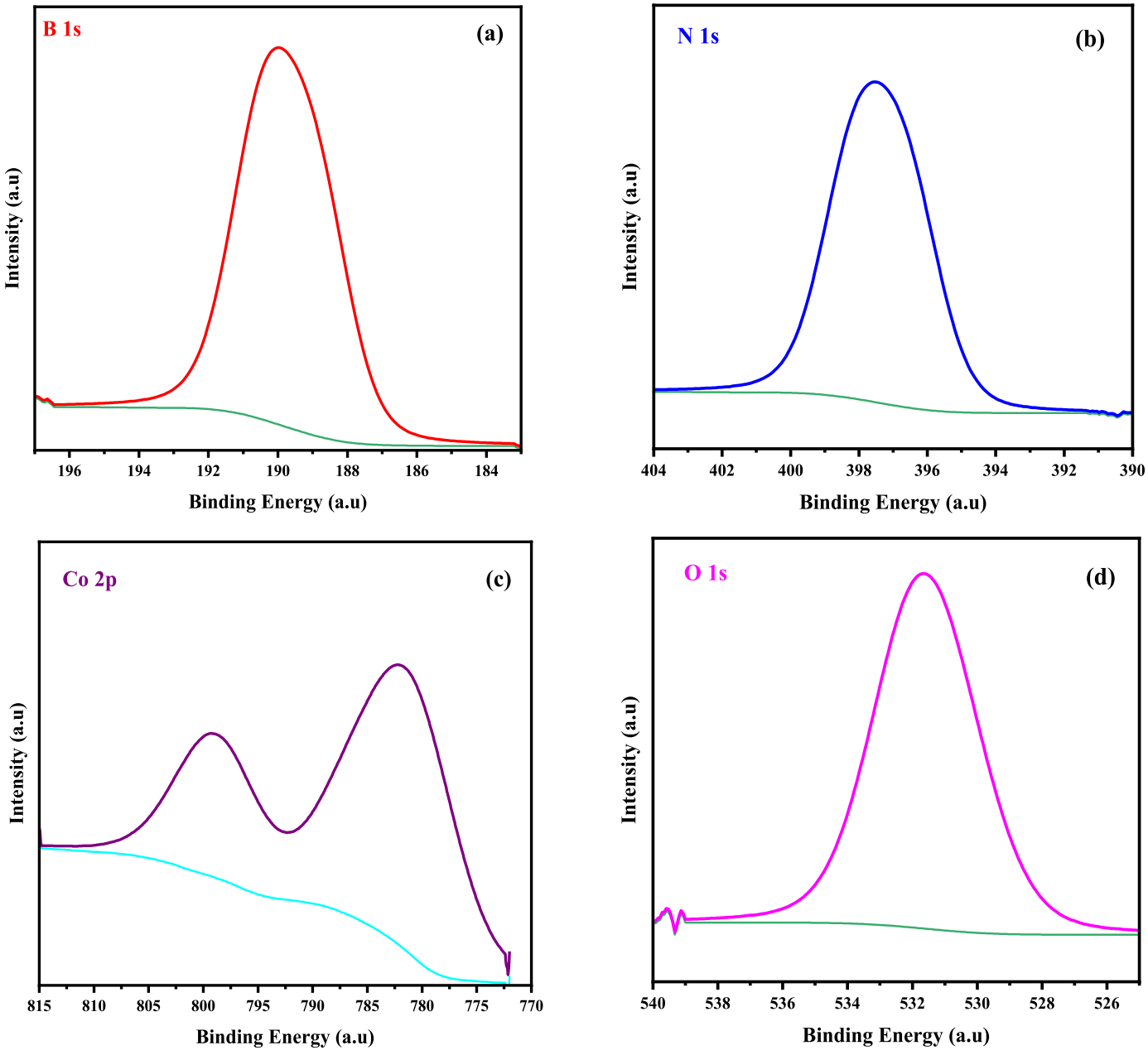

Fig. 2. High-resolution spectra of (**a**) B 1 s, (**b**), N 1s, (**c**) Co 2p, and (**d**) O 1s of 1% Co_3O_4-hBN composite, respectively.

indicative of Co^{2+} and Co^{3+} oxidation states, confirming the presence of Co_3O_4 in the composite (Biesinger et al., 2011). The O1s spectrum shows a notable difference between the pristine hBN and the 1% Co_3O_4-hBN composite. In pristine hBN (Fig. S8), the O1s peak is minimal, probably due to surface oxidation or adsorbed oxygen species. However, in the 1% Co_3O_4-hBN composite (Fig. 2d), the O1s peak at 531.2 eV is more evident, corresponding to the oxygen in Co_3O_4. This difference confirms the successful incorporation of Co_3O_4 into the hBN matrix. Likewise, the Co2p spectrum of Co_3O_4 (Fig. S9) displays two primary peaks corresponding to $Co2p_{3/2}$ and $Co2p_{1/2}$, located around 780 eV and 795 eV, respectively (Biesinger et al., 2011). Similarly, the O1s spectrum shows a primary peak around 529.5 eV, typically associated with lattice oxygen in metal oxides, like Co_3O_4 (Biesinger et al., 2011).

The SEM images provided detailed insights into the morphological characteristics of Co_3O_4, hBN, and 1%Co_3O_4-hBN materials, as shown in Fig. 3. The SEM images of Co_3O_4, depicted in Fig. 3a and b, show that the material consists of agglomerated nanoparticles. The granular texture observed suggests a high degree of aggregation, with individual particle sizes ranging from approximately 19 nm–26 nm, as measured in Fig. 3b. The SEM images of hBN, shown in Fig. 3c and d, exhibit a different morphology compared to pristine Co_3O_4, displaying a layered structure with well-defined, rounded, or spherical features, significantly larger than Co_3O_4 particles. Fig. 3c shows a relatively smooth and layered surface, typical of hBN (Kobayashi et al., 2012; Park and Seo, 2023). Fig. 3d shows a more detailed view of the hBN structure, showing densely packed layers.

The TEM images demonstrate the morphological characteristics of Co_3O_4, hBN, and 1% Co_3O_4-hBN composite. Fig. 3g shows Co_3O_4 nanoparticles as smaller, denser regions, while Fig. 3h exhibits the layered structure of hBN with lighter, larger areas. Fig. 3i and k presents the successful dispersion of Co_3O_4 nanoparticles on the hBN matrix in the 1% Co_3O_4-hBN composite, highlighting the effective integration of Co_3O_4 into the hBN framework.

3.2. Photocatalytic activity

3.2.1. MB degradation

The photocatalytic efficiency of the synthesized samples was evaluated by monitoring the discoloration of methylene blue (MB) under simulated sunlight irradiation at ambient temperature. The results, shown in Fig. 4a, compare the MB degradation both in the presence and in the absence (photolysis) of Co_3O_4/hBN composites. The findings indicate that, without any photocatalyst, MB degradation is negligible. Moreover, the adsorption experiments revealed that after 120 min, less than 8% of MB was adsorbed, suggesting that the further discoloration observed with Co_3O_4/hBN is primarily due to photocatalysis. When pristine hBN was used, less than 25% of MB was degraded after 120 min of illumination (Fig. 4a). Incorporating Co_3O_4 into the hBN enhanced the photocatalytic efficiency. In fact, the photodegradation efficiencies of 0.5% Co_3O_4/hBN, 1% Co_3O_4/hBN, and 2% Co_3O_4/hBN were 70%, 100%, and 84%, respectively, with the highest efficiency observed for the 1% Co_3O_4/hBN composite, which degraded ≈100% of MB in 120 min. When the Co_3O_4 loading was 5% the degradation of MB dropped to 54% in 120 min. These results suggest that the Co_3O_4 content is a critical factor in determining the photocatalytic efficiency of the composites, where adding Co_3O_4 to hBN increases activity, but excessive Co_3O_4 can have a detrimental effect. The optimal dispersion of Co_3O_4 on the hBN structure, facilitated by the appropriate Co_3O_4 concentration, enhances charge transfer and separation while maintaining surface accessibility for oxidation. Conversely, an excess of Co_3O_4 may obstruct access to oxidation sites due to surface coverage [63]. The kinetics of MB photodegradation in the presence of Co_3O_4/hBN composites were also studied, as described in Fig. 4b. The linear relationship between the degradation curve and illumination time indicates that MB photodegradation by Co_3O_4/hBN follows a pseudo-first-order reaction. Fig. 4b illustrates the apparent rate constant (k) for various Co_3O_4 amounts, with the highest k value of 0.020 min^{-1} observed for 1% Co_3O_4/hBN, which is 10 times higher than that of hBN (0.002 min^{-1}), confirming that an optimal Co_3O_4 amount significantly enhances photocatalytic activity. The results show that Co_3O_4 significantly enhances the photocatalytic degradation of MB when supported on hBN, with 1 wt% being the optimal loading.

Table 2 illustrates the photocatalytic degradation efficiency of Co_3O_4-hBN in comparison with other photocatalysts for MB under visible light. These results indicate that Co_3O_4-hBN is a promising photocatalyst for organic dye degradation, offering significant potential for environmental remediation applications, particularly in visible-light-driven processes.

3.2.2. IBF degradation

The photocatalytic degradation of IBF using hBN modified with various weight percentages of Co_3O_4 (0.5%, 1%, and 2%) was investigated. The results, illustrated in Fig. 4c, reveal an explicit dependency of the photocatalytic efficiency of the composites on the Co_3O_4 loading. As demonstrated in the control experiment (blank), the absence of any catalyst results in negligible degradation of IBF over 120 min, emphasizing the necessity of a catalytic system for efficient pollutant degradation. The hBN showed a degradation of approximately 20% after 120 min. This limited activity can be attributed to the intrinsic properties of hBN, which, despite its high thermal and chemical stability, lacks sufficient photocatalytic activity on its own. Upon doping hBN with 0.5% Co_3O_4, an enhancement in the degradation rate is observed. The IBF concentration decreases by approximately 60% within the first 60 min, indicating that adding Co_3O_4 significantly improves the photocatalytic activity. Also, in this case, the most pronounced catalytic activity is observed with 1% Co_3O_4 decorated material, where the concentration of IBF reduces to nearly 90% of its initial value within 120 min. However, increasing the Co_3O_4 concentration to 2% results in a decline in photocatalytic efficiency. While still more effective than pure hBN or lower Co_3O_4 loadings, the degradation rate at 2% Co_3O_4 is slower than that at 1%. This phenomenon may be attributed to the agglomeration of Co_3O_4 particles at higher concentrations, leading to a reduction in the overall surface area and, consequently, fewer accessible active sites for the catalytic reaction. Excessive Co_3O_4 may also cause increased light scattering, reducing effective photon absorption and lowering ROS generation. The higher performance of 1% Co_3O_4-decorated hBN suggests an optimal balance between the number of active sites and the effective dispersion of Co_3O_4 particles on the hBN surface. This likely maximizes the availability of catalytic sites while minimizing potential drawbacks such as particle aggregation, which can inhibit the accessibility of active sites. The kinetics of IBF photodegradation in the presence of Co_3O_4/hBN composites were also studied. Fig. 4d illustrates the apparent rate constant (k) for various Co_3O_4 amounts, with the highest k value of 0.015 min^{-1} observed for 1% Co_3O_4/hBN, which is 15 times higher than that of hBN (0.001 min^{-1}), confirming that an optimal Co_3O_4 amount significantly enhances photocatalytic activity.

Table 2 highlights the photocatalytic efficiency of Co_3O_4-hBN for ibuprofen degradation compared to other reported catalysts. It can be concluded that Co_3O_4-hBN exhibits a high % degradation efficiency of 90% under sunlight within 120 min, positioning it as an effective photocatalyst. This performance further indicates the potential of Co_3O_4-hBN for environmental applications in the photodegradation of pharmaceuticals like ibuprofen.

The enhanced photocatalytic activity observed for the Co_3O_4-decorated hBN can be explained by the synergistic effects between hBN and Co_3O_4. While hBN provides stable and high-surface-area support, Co_3O_4 interveners in active sites for generating reactive oxygen species ROS under light irradiation. The balance between these components is crucial: at lower Co_3O_4 concentrations, the dispersion is sufficient to maintain high activity. However, as the concentration increases, the potential for particle aggregation undermines the benefits of increased active site density.

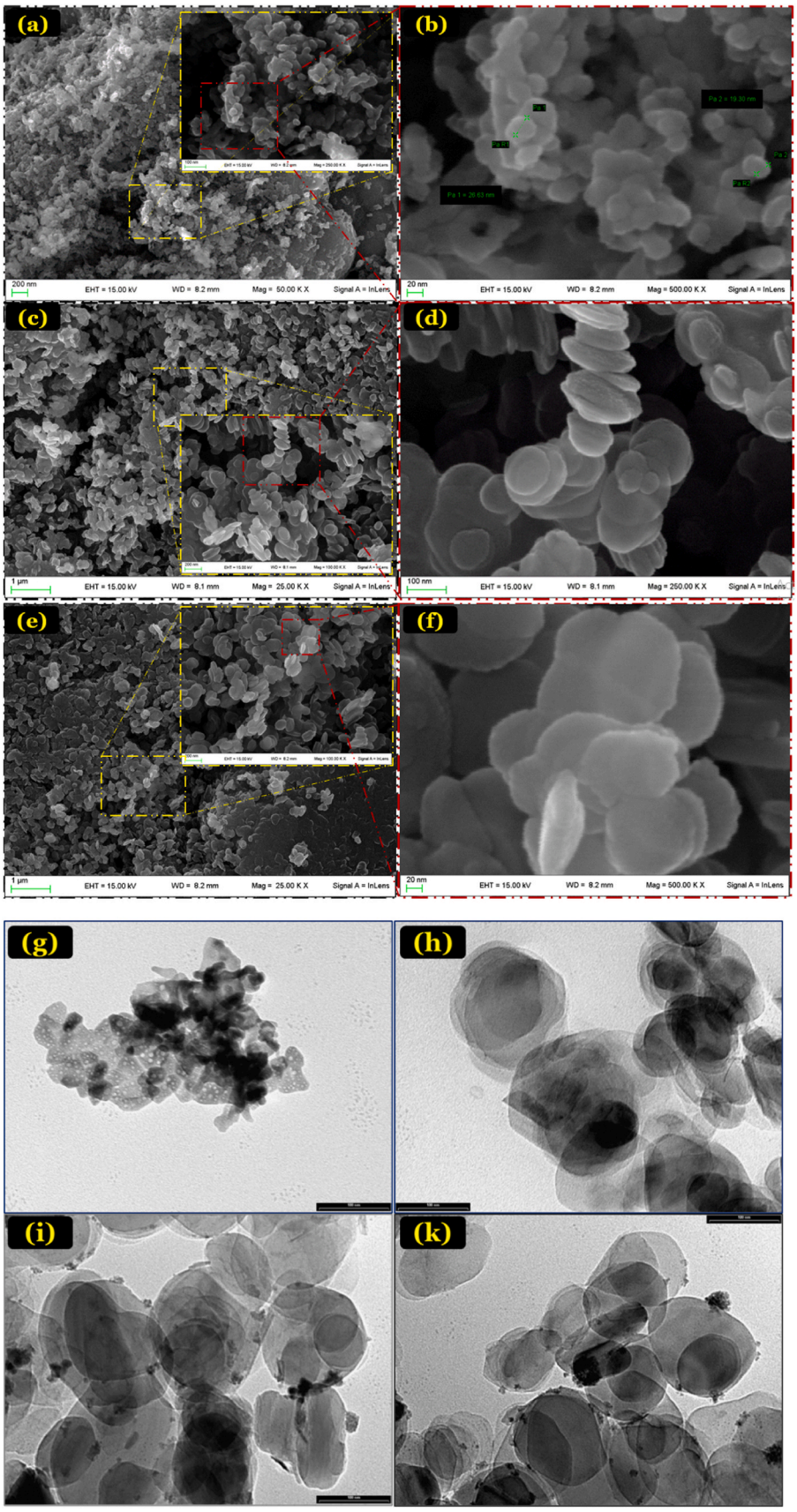

Fig. 3. SEM images of **(a,b)** Co_3O_4, **(c,d)** Boron nitiride, and **(e,f)** 1%Co_3O_4-BN. TEM images of **(g)** Co_3O_4, **(h)** hBN, and **(i,k)** 1%Co_3O_4-hBN.

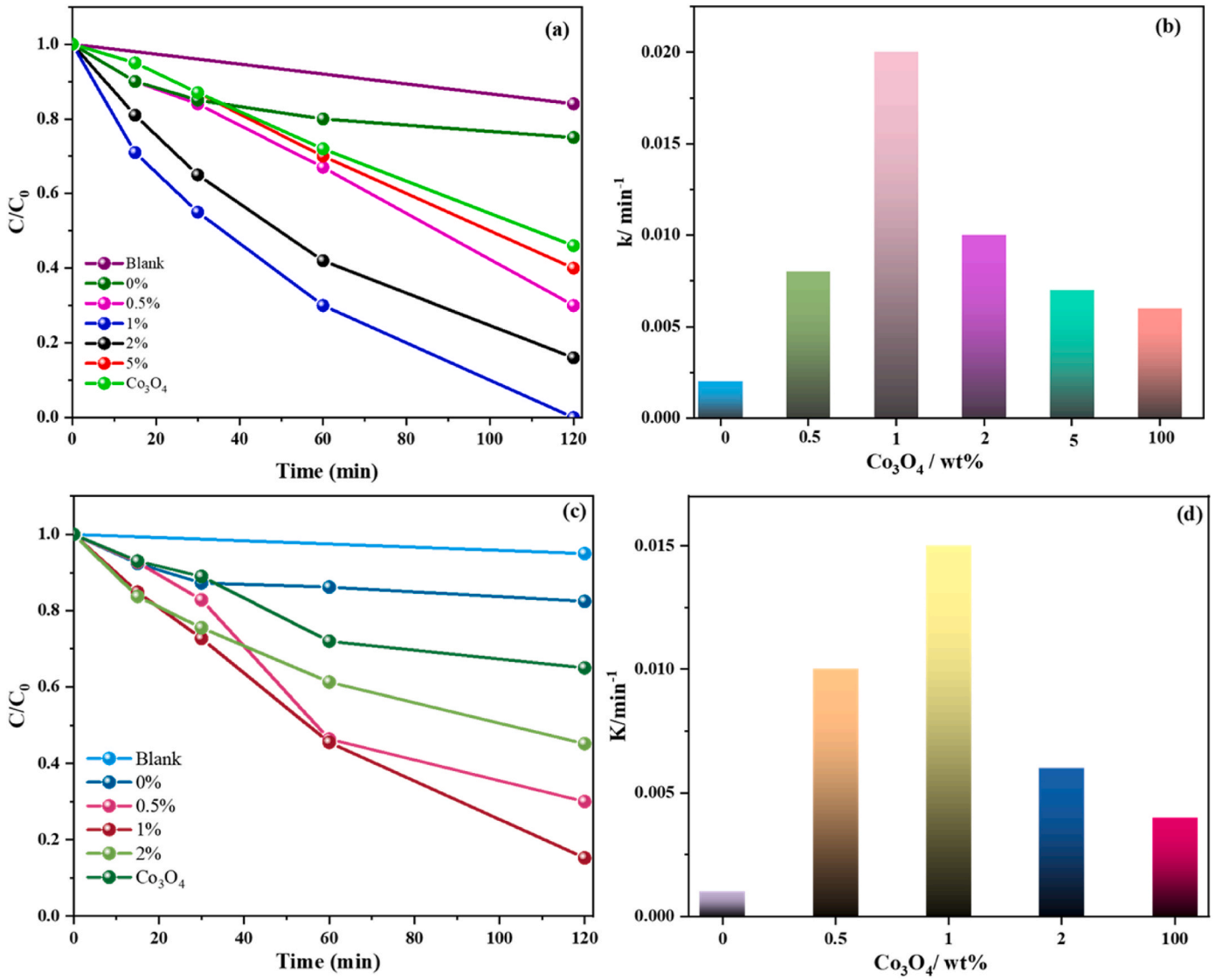

Fig. 4. (a) MB photodegradation by the prepared photocatalysts under sunlight illumination. (b) Rate constant (k, min^{-1}) of hBN, Co_3O_4 and Co_3O_4/hBN composites, (c) IBF photodegradation by the prepared photocatalysts under sunlight irradiation. (d) Rate constant of hBN, Co_3O_4 and Co_3O_4/hBN composites.

Table 2
Comparison of photocatalytic degradation performance of MB and IBF using different catalytic systems.

Photocatalyst	Organic pollutant	Light source	Degradation efficiency (%)	Degradation Time (min)	Reference
Fe_2O_3-BN	MB	Visible	66	180	Shenoy et al. (2021)
BN/Ag_3PO_4	MB	Visible	87.5	50	Zhu et al. (2016)
$FeVO_4$/hBN	MB	Visible	96.4	60	Sankeetha et al. (2023)
$Co_xZn_{1-x}Fe_2O_4$	MB	Visible	77	60	Chahar et al. (2021)
g–C_3N_4–Co_3O_4	MB	Visible	52.9	80	Palanisamy et al. (2021)
Co_3O_4-hBN	MB	Sunlight	100	120	This work
TiO_2	Ibuprofen	Solar light	100	300	Khedr et al. (2019)
$FePO_4$	Ibuprofen	Sunlight	97	120	Mimouni et al. (2022)
Bi_2O_4/Fe_3O_4	Ibuprofen	Visible light	100	120	Xia and Lo (2016)
Cu/$Bi_2Ti_2O_7$/rGO	Ibuprofen	Visible light	72.6	90	Shanavas et al. (2019)
TiO_2–Ru(II)	Ibuprofen	Visible light	64	300	Góngora et al. (2017)
Co_3O_4-hBN	Ibuprofen	Sunlight	90	120	This work

It is worth mentioning that MB exhibits a higher degradation rate than IBF due to several factors. MB, a large, charged dye, absorbs visible light efficiently, which enhances its interaction with the photocatalyst and accelerates degradation (Chen et al., 2020; Chen and Mao, 2007). In contrast, IBF is smaller and neutral, making it less prone to oxidative attack. Additionally, MB's strong light absorption results in higher excitation rates and more effective generation of ROS on the surface of the photocatalyst, whereas IBF absorbs less light and relies more on the catalyst for its degradation (Chen et al., 2020; Chen and Mao, 2007). Thus, the Co_3O_4/hBN photocatalyst performs more efficiently with MB due to these favorable molecular and optical properties.

3.3. Active species identification via radical scavenging experiments and stability

Fig. 5 illustrates the impact of various radical scavengers on the degradation efficiency of MB under photocatalytic conditions. The control experiment, conducted without any scavenger, exhibits near-complete removal of MB, indicating the high efficiency of the photocatalytic process. However, the introduction of scavengers results in a significant decrease in degradation efficiency. Chloroform (Chlo), which acts as a scavenger for superoxide radicals ($O_2^{\bullet -}$), significantly reduces MB removal, indicating the critical role of $O_2^{\bullet -}$ in the photocatalytic degradation process. IPA, known as •OH scavenger, also leads to a substantial decline in degradation efficiency, suggesting the involvement of •OH radicals in the process. Similarly, KI, which primarily traps h^+, results in a further decrease in MB degradation, highlighting the participation of h^+ in the photocatalytic mechanism. These results jointly establish that $O_2^{\bullet -}$, •OH, and h^+ are all reactive species involved in the photocatalytic degradation of MB, and their neutralization by scavengers leads to significant inhibition of the process.

The stability and re-usability of photocatalysts are important indices to measure their assessment and application. Thus, to further investigate the re-usability of the 1% Co_3O_4-hBN photocatalyst, it was recovered from the reaction mixture through filtration, rinsed thoroughly with deionized water, dried at 60 °C, and subsequently reused for four cycles.

As shown in Fig. 5b, the photocatalytic activity of the 1% Co_3O_4-hBN composite remained constant, indicating its effectiveness and stability during the photocatalytic process after 4 recycling runs under simulated sunlight.

To better demonstrate the structural stability of the 1% Co_3O_4-hBN composite photocatalyst, its structural characteristics before and after four consecutive recycling runs were examined using both XRD and SEM techniques, with the results illustrated in Fig. S10 and Fig. S11.

The XRD pattern of the recycled composite photocatalyst closely matches that of the fresh sample (Fig. S10), confirming that its crystalline structure remained intact throughout the reactions. Furthermore, SEM analysis (Fig. S11) revealed no apparent alterations in the material's morphology, highlighting its robust structural integrity even after several cycles of use.

3.4. Proposed mechanism

The photocatalytic activity of 1% Co_3O_4-hBN composite was systematically investigated through radical scavenger experiments, showing that $O_2^{\bullet -}$ and •OH play roles in the photocatalytic performance. The proposed mechanism is given in Fig. 6. Upon visible light irradiation, Co_3O_4 absorbs photons, generating electron-hole pairs (e^-/h^+) (Eq. (3)). The photogenerated electrons in the conduction band of Co_3O_4 are transferred to hBN, where they effectively reduce O_2 to form $O_2^{\bullet -}$ (Eq. (4)). Simultaneously, the photogenerated holes in the valence band of Co_3O_4 either contribute to directly oxidizing water molecules and generate •OH (Eq. (5)) or oxidize hydroxide ions OH^- to yield additional hydroxyl radicals (Eq. (6)). These reactive oxygen species, particularly O_2•− and •OH, are the primary agents responsible for the oxidative degradation of MB, leading to its eventual mineralization, a process similarly reported in the literature (Wang et al., 2018). The scavenger experiments confirmed the involvement of O_2•−, supporting the proposed mechanism and highlighting the synergistic effect between Co_3O_4 and hBN in enhancing photocatalytic efficiency.

$$1\%\ Co_3O_4 - hBN + h\nu \longrightarrow 1\%Co_3O_4 - hBN\ (e^- + h^+) \quad (3)$$

$$O_2 + e^- \longrightarrow O_2^- \quad (4)$$

$$H_2O + h^+ \longrightarrow OH^{\cdot} + H^+ \quad (5)$$

$$OH^- + h^+ \longrightarrow OH^{\cdot} \quad (6)$$

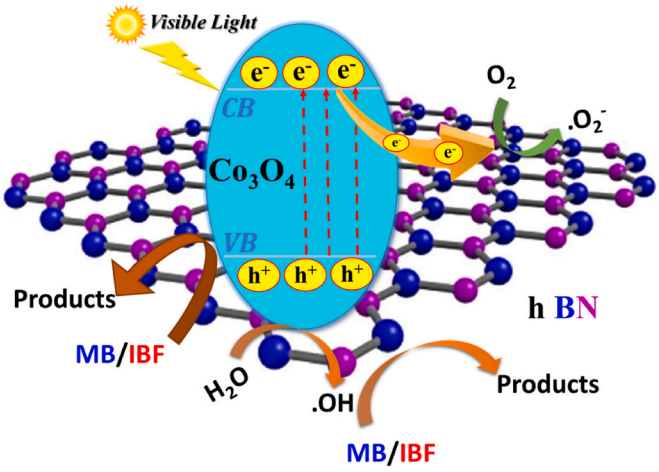

Fig. 6. Proposed mechanism for MB and IBF degradation using 1% Co_3O_4-hBN.

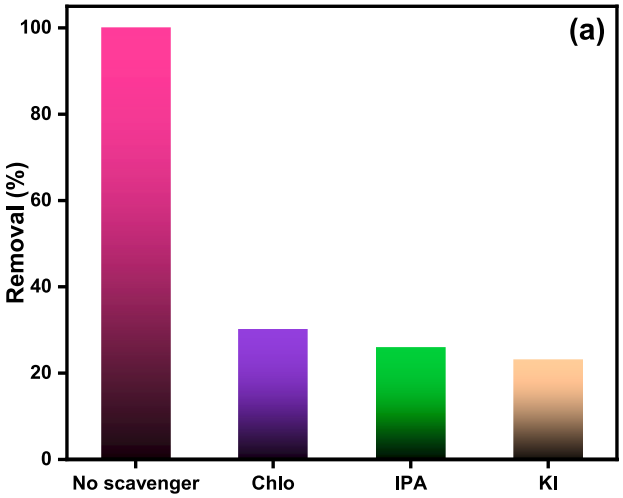

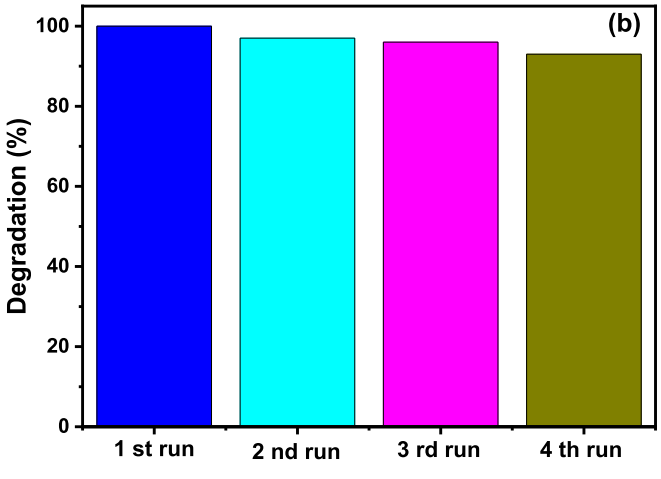

Fig. 5. (a) MB photocatalytic degradation by 1% Co_3O_4-hBN composite under simulated sunlight in the presence of scavengers: KI, IPA, and chloroform and **(b)** Reuse test of 1% Co_3O_4-hBN composite in MB photocatalytic degradation.

3.5. Electrical energy determination

The photochemical process of degradation of MB and IBF is an electrical energy-intensive process. This electrical energy represents a major fraction of the total operating cost. The E_{EO} for batch-type reaction can be calculated by using the equation below (Vishnuganth et al., 2016).

$$E_{EO} = \frac{\mathbf{P} \times \mathbf{t} \times \mathbf{1000}}{\mathbf{V} \times \mathbf{60} \times \mathbf{log}\left(\frac{C_0}{C_f}\right)} \quad \text{Eq. 7}$$

$$\ln\left(\frac{C}{C_0}\right) = -K_{app} \times t \quad \text{Eq.8}$$

where P is the rated power (kW) of the AOP system, t is the irradiation time (min), V is the volume (l) of the water in the reactor, C_0 and C are the initial and final pollutant concentrations and k_{app} is the pseudo-first-order rate constant (min^{-1}) for the decay of the pollutant concentration.

So by combining Eq. 7 and the L-H first-order kinetics (Eq. (8), we can express the E_{EO} as

$$E_{EO} = \frac{\mathbf{38.4} \times \mathbf{P}}{\mathbf{V} \times \boldsymbol{K_{app}}} \quad \text{Eq. 9}$$

The electric energy (kWh m^{-3}) required for removing 10 mg/L of MB or IBF from 100 mL of polluted solution has been given in Table S.1. The E_{EO} values indicated that the required electrical energy for photocatalysis of poluants was in the following order: hBN > Co_3O_4 > 1% Co_3O_4-hBN.

Finally, it is useful to relate the E_{EO} values found in this study to treatment costs. If the cost of electricity, in Turkey, is $ 0.045 (taxes included) per kWh, the contribution to treatment cost from electrical energy in case, for example, of the removal of MB dye will be $ 256.5, 864, 2160 per m^3, in the presence of the catalyst 1% Co_3O_4-hBN, Co_3O_4 and hBN respectively. Notably, this study was conducted under solar irradiation, which substantially reduced the operational cost of the treatment. In contrast, other studies employed external energy sources, leading to higher operational costs.

4. Conclusion

In this study, we successfully synthesized and characterized Co_3O_4-hBN composites using a dry impregnation method. The integration of Co_3O_4 on the hBN matrix aimed to enhance the photocatalytic performance of hBN, particularly under visible light irradiation, by taking advantage of Co_3O_4's narrow bandgap and its ability to absorb visible light effectively. Through proper analytical investigations, we demonstrated that Co_3O_4 was successfully incorporated into the hBN structure, resulting in important changes in the optical and electronic properties of the composite material. The optimized 1% (wt%) Co_3O_4 loading in hBN exhibited the most enhanced photocatalytic activity, achieving nearly complete degradation of MB within 60 min and significant degradation of IBF after 120 min under simulated sunlight. The enhanced photocatalytic performance of 1% Co_3O_4-hBN composite can be attributed to the synergistic interaction between hBN and Co_3O_4. The coupling of these two materials broadens the light absorption spectrum and promotes efficient charge separation, which is crucial for improving the photocatalytic degradation of organic pollutants. These findings emphasize the potential of Co_3O_4-hBN composites as effective photocatalysts for environmental remediation, particularly in harnessing solar energy for the degradation of persistent organic pollutants. Moreover, the results from this study provide valuable insights into the design and development of hBN-based photocatalysts with enhanced visible light activity. The successful incorporation of Co_3O_4 into hBN offers a promising strategy for extending the photocatalytic applications of hBN beyond the UV range, paving the way for more sustainable and efficient photocatalytic processes.

CRediT authorship contribution statement

Mariam Bouziani: Writing – original draft, Investigation, Formal analysis, Conceptualization. **Asmae Bouziani:** Writing – review & editing, Methodology, Data curation, Conceptualization. **Abdelghani Hsini:** Writing – review & editing, Investigation, Data curation. **Claudia L. Bianchi:** Writing – review & editing, Resources, Data curation. **Ermelinda Falletta:** Writing – review & editing, Resources, Investigation, Data curation. **Alessandro Di Michele:** Writing – review & editing, Resources, Formal analysis. **Gökhan Çelik:** Writing – review & editing, Resources, Data curation. **Robert Hausler:** Writing – review & editing, Supervision, Resources.

Declaration of competing interest

The authors declare that they have no known competing financial interests or personal relationships that could have appeared to influence the work reported in this paper.

Appendix A. Supplementary data

Supplementary data to this article can be found online at https://doi.org/10.1016/j.chemosphere.2025.144061.

Data availability

Data will be made available on request.

References

Afzal, S., Rehman, A. ur, Najam, T., Hossain, I., Abdelmotaleb, M.A.I., Riaz, S., Karim, M. R., Shah, S.S.A., Nazir, M.A., 2024. Recent advances of MXene@MOF composites for catalytic water splitting and wastewater treatment approaches. Chemosphere 364, 143194. https://doi.org/10.1016/J.CHEMOSPHERE.2024.143194.

Ahmad, U., Ullah, Sami, Rehman, A., Najam, T., Alarfaji, S.S., Jamshaid, M., Parkash Kumar, O., Ullah, Sultan, Shahid, M., Ahmad Shah, S.S., Altaf Nazir, M., 2024. ZIF-8 composites for the removal of wastewater pollutants. ChemistrySelect 9, e202401719. https://doi.org/10.1002/SLCT.202401719.

Anum, A., Ibrahim, S.M., Tahir, A.A., Nazir, M.A., Malik, M., Shah, S.S.A., Ehsan, A., Wattoo, M.A., Rehman, A. ur, 2023. Construction of hybrid sulfur-doped MOF-235@g-C_3N_4 photocatalyst for the efficient removal of nicotine. Inorg. Chem. Commun. 157, 111268. https://doi.org/10.1016/J.INOCHE.2023.111268.

Anum, A., Nazir, M.A., Shah, S.S.A., Elnaggar, A.Y., Mahmoud, M.H.H., El-Bahy, S.M., Malik, M., Wattoo, M.A., Rehman, A. ur, 2024. Advanced Nix/MoSx/MOF-2@g-C_3N_4 carbon nanostructures for the effective eradication of the Methylene blue dye. Fullerenes, Nanotub. Carbon Nanostruct. https://doi.org/10.1080/1536383X.2024.2372407.

Biesinger, M.C., Payne, B.P., Grosvenor, A.P., Lau, L.W.M., Gerson, A.R., Smart, R.S.C., 2011. Resolving surface chemical states in XPS analysis of first row transition metals, oxides and hydroxides: Cr, Mn, Fe, Co and Ni. Appl. Surf. Sci. 257, 2717–2730. https://doi.org/10.1016/J.APSUSC.2010.10.051.

Chahar, D., Taneja, S., Bisht, S., Kesarwani, S., Thakur, P., Thakur, A., Sharma, P.B., 2021. Photocatalytic activity of cobalt substituted zinc ferrite for the degradation of methylene blue dye under visible light irradiation. J. Alloys Compd. 851, 156878. https://doi.org/10.1016/J.JALLCOM.2020.156878.

Chen, D., Cheng, Y., Zhou, N., Chen, P., Wang, Y., Li, K., Huo, S., Cheng, P., Peng, P., Zhang, R., Wang, L., Liu, H., Liu, Y., Ruan, R., 2020. Photocatalytic degradation of organic pollutants using TiO_2-based photocatalysts: a review. J. Clean. Prod. 268, 121725. https://doi.org/10.1016/J.JCLEPRO.2020.121725.

Chen, X., Mao, S.S., 2007. Titanium dioxide nanomaterials: synthesis, properties, modifications and applications. Chem. Rev. 107, 2891–2959. https://doi.org/10.1021/CR0500535.

Eleryan, A., Hassaan, M., Nazir, M.A., Shah, S.S.A., Ragab, S., El Nemr, A., 2024. Isothermal and kinetic screening of methyl red and methyl orange dyes adsorption from water by Delonix regia biochar-sulfur oxide (DRB-SO). Scientific Reports 2024 14 (1 14), 1–16. https://doi.org/10.1038/s41598-024-63510-0.

Fu, X., Hu, Y., Yang, Y., Liu, W., Chen, S., 2013. Ball milled h-BN: an efficient holes transfer promoter to enhance the photocatalytic performance of TiO_2. J. Hazard Mater. 244–245, 102–110. https://doi.org/10.1016/J.JHAZMAT.2012.11.033.

Gao, G., Mathkar, A., Martins, E.P., Galvão, D.S., Gao, D., Alves Da Silva Autreto, P., Sun, C., Cai, L., Ajayan, P.M., 2014. Designing nanoscaled hybrids from atomic layered boron nitride with silver nanoparticle deposition. J Mater Chem A Mater 2, 3148–3154. https://doi.org/10.1039/C3TA12892J.

Góngora, J.F., Elizondo, P., Hernández-Ramírez, A., 2017. Photocatalytic degradation of ibuprofen using TiO_2 sensitized by Ru(ii) polyaza complexes. Photochem. Photobiol. Sci. 16, 31–37. https://doi.org/10.1039/C6PP00222F.

Grant, J.T., Carrero, C.A., Goeltl, F., Venegas, J., Mueller, P., Burt, S.P., Specht, S.E., McDermott, W.P., Chieregato, A., Hermans, I., 2016. Selective oxidative dehydrogenation of propane to propene using boron nitride catalysts. Science 354 (1979), 1570–1573. https://doi.org/10.1126/science.aaf7885.

Hashimoto, K., Irie, H., Fujishima, A., 2005. TiO 2 photocatalysis: a historical overview and future prospects. Jpn. J. Appl. Phys., Part 1: Regular Papers and Short Notes and Review Papers 44, 8269–8285. https://doi.org/10.1143/JJAP.44.8269.

Herrmann, J.M., 1999. Heterogeneous photocatalysis: fundamentals and applications to the removal of various types of aqueous pollutants. Catal. Today 53, 115–129. https://doi.org/10.1016/S0920-5861(99)00107-8.

Hoffmann, M.R., Martin, S.T., Choi, W., Bahnemann, D.W., 1995. Environmental applications of semiconductor photocatalysis. Chem. Rev. 95, 69–96. https://doi.org/10.1021/cr00033a004.

Jaramillo-Páez, C., Navío, J.A., Hidalgo, M.C., Bouziani, A., Azzouzi, M. El, 2017. Mixed α-Fe_2O_3/Bi_2WO_6 oxides for photoassisted hetero-Fenton degradation of Methyl Orange and Phenol. J. Photochem. Photobiol. Chem. 332, 521–533. https://doi.org/10.1016/J.JPHOTOCHEM.2016.09.031.

Jimenéz-Calvo, P., Naciri, Y., Sobolewska, A., Isaacs, M., Zhang, Y., Leforestier, A., Degrouard, J., Rouzière, S., Goldmann, C., Vantelon, D., Hettler, S., Zaluzec, N.J., Arenal, R., Launois, P., Ghazzal, M.N., Paineau, E., 2024. Ti-modified imogolite nanotubes as promising photocatalyst 1D nanostructures for H_2 production. Small Methods 8, 2301369. https://doi.org/10.1002/SMTD.202301369.

Kadian, A., Manikandan, V., Chen, C.L., Dong, C.L., Annapoorni, S., 2024. Synergistically enhanced photocatalytic properties of Co_3O_4-G/GO nanocomposites: unravelling their interactions and charge-transfer dynamics using XAS. Dalton Trans. 53, 13550–13565. https://doi.org/10.1039/D4DT01405G.

Khalil, A., Nazir, M.A., Salem, M.A., Ragab, S., El Nemr, A., 2024. Magnetic pomegranate peels activated carbon (MG-PPAC) composite for Acid Orange 7 dye removal from wastewater. Appl. Water Sci. 14, 1–16. https://doi.org/10.1007/S13201-024-02225-Z.

Khedr, T.M., El-Sheikh, S.M., Ismail, A.A., Bahnemann, D.W., 2019. Highly efficient solar light-assisted TiO_2 nanocrystalline for photodegradation of ibuprofen drug. Opt. Mater. 88, 117–127. https://doi.org/10.1016/J.OPTMAT.2018.11.027.

Kobayashi, Y., Kumakura, K., Akasaka, T., Makimoto, T., 2012. Layered boron nitride as a release layer for mechanical transfer of GaN-based devices. Nature 484, 223–227. https://doi.org/10.1038/NATURE10970.

Li, X., Yu, J., Wageh, S., Al-Ghamdi, A.A., Xie, J., 2016. Graphene in photocatalysis: a review. Small 12, 6640–6696. https://doi.org/10.1002/SMLL.201600382.

Liu, J., Wang, D., Wang, M., Kong, D., Zhang, Y., Chen, J.F., Dai, L., 2016. Uniform two-dimensional Co_3O_4 porous sheets: facile synthesis and enhanced photocatalytic performance. Chem. Eng. Technol. 39, 891–898. https://doi.org/10.1002/CEAT.201500542.

Liu, Q., Chen, C., Du, M., Wu, Y., Ren, C., Ding, K., Song, M., Huang, C., 2018. Porous hexagonal boron nitride sheets: effect of hydroxyl and secondary amino groups on photocatalytic hydrogen evolution. ACS Appl. Nano Mater. 1, 4566–4575. https://doi.org/10.1021/ACSANM.8B00867.

Malik, M., Ibrahim, S.M., Nazir, M.A., Tahir, A.A., Tufail, M.K., Shah, S.S.A., Anum, A., Wattoo, M.A., Rehman, A. ur, 2023. Engineering of a hybrid g-C_3N_4/ZnO-W/cox heterojunction photocatalyst for the removal of methylene blue dye. Catalysts 2023 13, 813. https://doi.org/10.3390/CATAL13050813. Page 813 13.

Mimouni, I., Yahya, M., Bouziani, A., Naciri, Y., Maarouf, F. ezzahra, Alaoui El Belghiti, M., El Azzouzi, M., 2022. Iron phosphate for photocatalytic removal of Ibuprofen from aqueous media under sun-like irradiation. J. Photochem. Photobiol. Chem. 433, 114170. https://doi.org/10.1016/J.JPHOTOCHEM.2022.114170.

Naciri, Y., Ghazzal, M.N., Paineau, E., 2024. Nanosized tubular clay minerals as inorganic nanoreactors for energy and environmental applications: a review to fill current knowledge gaps. Adv. Colloid Interface Sci. 326, 103139. https://doi.org/10.1016/J.CIS.2024.103139.

Naciri, Y., Hsini, A., Ahdour, A., Akhsassi, B., Fritah, kamal, Ajmal, Z., Djellabi, R., Bouziani, A., Taoufyq, A., Bakiz, B., Benlhachemi, A., Sillanpää, M., Li, H., 2022. Recent advances of bismuth titanate based photocatalysts engineering for enhanced organic contaminates oxidation in water: a review. Chemosphere 300, 134622. https://doi.org/10.1016/J.CHEMOSPHERE.2022.134622.

Nakamoto, K., 2008. Infrared and Raman Spectra of Inorganic and Coordination Compounds: Part A: Theory and Applications in Inorganic Chemistry, sixth ed. Infrared and Raman Spectra of Inorganic and Coordination Compounds: Part A: Theory and Applications in Inorganic Chemistry, pp. 1–419. https://doi.org/10.1002/9780470405840.

Nazari, S., Zarealiabadi, H., Mansouri, M., Maleki, B., Bayati, B., 2024. The removal of methylene blue from aqueous solution using prepared ZSM-5 zeolite@ZnO nanoflowers under LED irradiation. Iran. J. Chem. Chem. Eng. (Int. Engl. Ed.) 43, 621–634. https://doi.org/10.30492/IJCCE.2023.2003412.6052.

Nazir, M.A., Ullah, S., Shahid, M.U., Hossain, I., Najam, T., Ismail, M.A., Rehman, A. ur, Karim, M.R., Shah, S.S.A., 2025. Zeolitic imidazolate frameworks (ZIF-8 & ZIF-67): synthesis and application for wastewater treatment. Sep. Purif. Technol. 356, 129828. https://doi.org/10.1016/J.SEPPUR.2024.129828.

Palanisamy, G., Bhuvaneswari, K., Srinivasan, M., Vignesh, S., Elavarasan, N., Venkatesh, G., Pazhanivel, T., Ramasamy, P., 2021. Two-dimensional g-C_3N_4 nanosheets supporting Co_3O_4-V_2O_5 nanocomposite for remarkable photodegradation of mixed organic dyes based on a dual Z-scheme photocatalytic system. Diam. Relat. Mater. 118, 108540. https://doi.org/10.1016/J.DIAMOND.2021.108540.

Park, A.H., Seo, T.H., 2023. Hexagonal boron nitride as an intermediate layer for gallium nitride epitaxial growth in near-ultraviolet light-emitting diodes. Materials 2023 16, 7216. https://doi.org/10.3390/MA16227216. Page 7216 16.

Prabaharan, D.D.M., Sadaiyandi, K., Mahendran, M., Sagadevan, S., 2017. Precipitation method and characterization of cobalt oxide nanoparticles. Appl. Phys. Mater. Sci. Process 123, 1–6. https://doi.org/10.1007/S00339-017-0786-8.

Qanbarzadeh, M., DiGiacomo, L., Bouteh, E., Alhamdan, E.Z., Mason, M.M., Wang, B., Wong, M.S., Cates, E.L., 2023. An ultraviolet/boron nitride photocatalytic process efficiently degrades poly-/perfluoroalkyl substances in complex water matrices. Environ. Sci. Technol. Lett. 10, 705–710. https://doi.org/10.1021/ACS.ESTLETT.3C00363.

Rana, A.K., Patel, M., Nguyen, T.T., Yun, J.H., Kim, J., 2020. Transparent Co_3O_4/ZnO photovoltaic broadband photodetector. Mater. Sci. Semicond. Process. 117, 105192. https://doi.org/10.1016/J.MSSP.2020.105192.

Roy, S., Zhang, X., Puthirath, A.B., Meiyazhagan, A., Bhattacharyya, S., Rahman, M.M., Babu, G., Susarla, S., Saju, S.K., Tran, M.K., Sassi, L.M., Saadi, M.A.S.R., Lai, J., Sahin, O., Sajadi, S.M., Dharmarajan, B., Salpekar, D., Chakingal, N., Baburaj, A., Shuai, X., Adumbumkulath, A., Miller, K.A., Gayle, J.M., Ajnsztajn, A., Prasankumar, T., Harikrishnan, V.V.J., Ojha, V., Kannan, H., Khater, A.Z., Zhu, Z., Iyengar, S.A., Autreto, P.A. da S., Oliveira, E.F., Gao, G., Birdwell, A.G., Neupane, M. R., Ivanov, T.G., Taha-Tijerina, J., Yadav, R.M., Arepalli, S., Vajtai, R., Ajayan, P.M., 2021. Structure, properties and applications of two-dimensional hexagonal boron nitride. Adv. Mater. 33, 2101589. https://doi.org/10.1002/ADMA.202101589.

Rueda-Marquez, J.J., Levchuk, I., Fernández Ibañez, P., Sillanpää, M., 2020. A critical review on application of photocatalysis for toxicity reduction of real wastewaters. J. Clean. Prod. https://doi.org/10.1016/j.jclepro.2020.120694.

Sankeetha, S., Muralidharan, R., Abirami, N., Arulmozhi, R., 2023. The synergetic action of $FeVO_4$ and h-BN for decontamination of industrial wastewater pollutants and the assessment of phytotoxicity. Ceram. Int. 49, 35847–35859. https://doi.org/10.1016/J.CERAMINT.2023.08.266.

Shah, S.S.A., Sohail, M., Murtza, G., Waseem, A., Rehman, A. ur, Hussain, I., Bashir, M.S., Alarfaji, S.S., Hassan, A.M., Nazir, M.A., Javed, M.S., Najam, T., 2024. Recent trends in wastewater treatment by using metal-organic frameworks (MOFs) and their composites: a critical view-point. Chemosphere 349, 140729. https://doi.org/10.1016/J.CHEMOSPHERE.2023.140729.

Shahid, M.U., Najam, T., Islam, M., Hassan, A.M., Assiri, M.A., Rauf, A., Rehman, A. ur, Shah, S.S.A., Nazir, M.A., 2024. Engineering of metal organic framework (MOF) membrane for waste water treatment: synthesis, applications and future challenges. J. Water Proc. Eng. 57, 104676. https://doi.org/10.1016/J.JWPE.2023.104676.

Shanavas, S., Priyadharsan, A., Gkanas, E.I., Acevedo, R., Anbarasan, P.M., 2019. High efficient catalytic degradation of tetracycline and ibuprofen using visible light driven novel Cu/$Bi_2Ti_2O_7$/rGO nanocomposite: kinetics, intermediates and mechanism. J. Ind. Eng. Chem. 72, 512–528. https://doi.org/10.1016/J.JIEC.2019.01.008.

Shen, T., Liu, S., Yan, W., Wang, J., 2019. Highly efficient preparation of hexagonal boron nitride by direct microwave heating for dye removal. J. Mater. Sci. 54, 8852–8859. https://doi.org/10.1007/S10853-019-03514-8.

Sheng, Y., Yang, J., Wang, F., Liu, L., Liu, H., Yan, C., Guo, Z., 2019. Sol-gel synthesized hexagonal boron nitride/titania nanocomposites with enhanced photocatalytic activity. Appl. Surf. Sci. 465, 154–163. https://doi.org/10.1016/J.APSUSC.2018.09.137.

Shenoy, M.R., Ayyasamy, S., Bhojan, V., Swaminathan, R., Raju, N., Senthil Kumar, P., Sasikumar, M., Kadarkarai, G., Tamilarasan, S., Thangavelu, S., J, S., Reddy, M.V., 2021. Visible light sensitive hexagonal boron nitride (hBN) decorated Fe_2O_3 photocatalyst for the degradation of methylene blue. J. Mater. Sci. Mater. Electron. 32, 4766–4783. https://doi.org/10.1007/S10854-020-05215-4.

Shiraishi, M., Inagaki, M., 2003. X-Ray diffraction methods to study crystallite size and lattice constants of carbon materials. Carbon Alloys: Novel Concepts to Develop Carbon Science and Technology 161–173. https://doi.org/10.1016/B978-008044163-4/50010-3.

Subagyo, R., Yudhowijoyo, A., Sholeha, N.A., Hutagalung, S.S., Prasetyoko, D., Birowosuto, M.D., Arramel, A., Jiang, J., Kusumawati, Y., 2023. Recent advances of modification effect in Co_3O_4-based catalyst towards highly efficient photocatalysis. J. Colloid Interface Sci. 650, 1550–1590. https://doi.org/10.1016/J.JCIS.2023.07.117.

Thommes, M., Kaneko, K., Neimark, A.V., Olivier, J.P., Rodriguez-Reinoso, F., Rouquerol, J., Sing, K.S.W., 2015. Physisorption of gases, with special reference to the evaluation of surface area and pore size distribution (IUPAC Technical Report). Pure Appl. Chem. 87, 1051–1069. https://doi.org/10.1515/PAC-2014-1117/MACHINEREADABLECITATION/RIS.

Ullah, S., Najam, T., Rehman, A. ur, Alarfaji, S.S., Ahmad, M.A., Riaz, S., Akkinepally, B., Shah, S.S.A., Nazir, M.A., 2024. MXene nanomaterials: synthesis, properties and applications in energy and environment sector. J. Alloys Compd. 1001, 175172. https://doi.org/10.1016/J.JALLCOM.2024.175172.

Vishnuganth, M.A., Remya, N., Kumar, M., Selvaraju, N., 2016. Photocatalytic degradation of carbofuran by TiO_2-coated activated carbon: model for kinetic, electrical energy per order and economic analysis. J. Environ. Manag. 181, 201–207. https://doi.org/10.1016/J.JENVMAN.2016.06.016.

Wang, G., Shen, X., Horvat, J., Wang, B., Liu, H., Wexler, D., Yao, J., 2009. Hydrothermal synthesis and optical, magnetic, and supercapacitance properties of nanoporous cobalt oxide nanorods. J. Phys. Chem. C 113, 4357–4361. https://doi.org/10.1021/JP8106149.

Wang, N., Yang, G., Wang, H., Sun, R., Wong, C.P., 2018. Visible light-responsive photocatalytic activity of boron nitride incorporated composites. Front. Chem. 6, 409908. https://doi.org/10.3389/FCHEM.2018.00440/BIBTEX.

Xia, D., Lo, I.M.C., 2016. Synthesis of magnetically separable Bi_2O_4/Fe_3O_4 hybrid nanocomposites with enhanced photocatalytic removal of ibuprofen under visible

light irradiation. Water Res. 100, 393–404. https://doi.org/10.1016/J.WATRES.2016.05.026.

Zhang, H.X., Shin, B.G., Lee, D.E., Yoon, K.B., 2020. Preparation of PP/2D-Nanosheet composites using MoS_2/$MgCl_2$- and BN/$MgCl_2$-bisupported ziegler–natta catalysts. Catalysts 2020 10. https://doi.org/10.3390/CATAL10060596. Page 596 10, 596.

Zhang, K., Feng, Y., Wang, F., Yang, Z., Wang, J., 2017. Two dimensional hexagonal boron nitride (2D-hBN): synthesis, properties and applications. J Mater Chem C Mater 5, 11992–12022. https://doi.org/10.1039/C7TC04300G.

Zhao, F., Ma, H., 2023. Application of Co_3O_4 in photoelectrocatalytic treatment of wastewater polluted with organic compounds: a review. Crystals 2023 13, 634. https://doi.org/10.3390/CRYST13040634. Page 634 13.

Zhou, C., Lai, C., Zhang, C., Zeng, G., Huang, D., Cheng, M., Hu, L., Xiong, W., Chen, M., Wang, J., Yang, Y., Jiang, L., 2018. Semiconductor/boron nitride composites: synthesis, properties, and photocatalysis applications. Appl. Catal., B 238, 6–18. https://doi.org/10.1016/J.APCATB.2018.07.011.

Zhou, J., Duo, F., Wang, C., Chu, L., Zhang, M., Yan, D., 2022. Robust photocatalytic activity of two-dimensional h-BN/Bi_2O_3 heterostructure quantum sheets. RSC Adv. 12, 13535–13547. https://doi.org/10.1039/D2RA02115C.

Zhu, C., Zheng, J., Fang, L., Hu, P., Liu, Y., Cao, X., Wu, M., 2016. Advanced visible-light driven photocatalyst with enhanced charge separation fabricated by facile deposition of Ag_3PO_4 nanoparticles on graphene-like h-BN nanosheets. J. Mol. Catal. Chem. 424, 135–144. https://doi.org/10.1016/J.MOLCATA.2016.08.028.